MONOCHROMATIC COMPUTED TOMOGRAPHY OF THE HUMAN BRAIN
USING SYNCHROTRON X RAYS: TECHNICAL FEASIBILITY

E. Nachaliel, F.A. Dilmanian, R.F. Garrett[1], W.C. Thomlinson,
L.D. Chapman, N.F. Gmür, N.M. Lazarz, H.R. Moulin[2],
M.L. Rivers, H. Rarback, P.M. Stefan, and P. Spanne

BNL--47068

DE92 007143

Brookhaven National Laboratory, Upton, NY 11973

P.N. Luke, R. Pehl, and A.C. Thompson
Lawrence Berkeley Laboratory, Berkeley, CA 94720

M. Miller
Analogic Corp., Peabody, MA 01960

ABSTRACT

A monochromatic computed tomography (CT) scanner is being developed at
the X17 superconducting wiggler beamline at the National Synchrotron Light
Source (NSLS), Brookhaven National Laboratory, to image the human head and
neck. The system configuration is one of a horizontal fan beam and an upright
seated rotating subject. The purposes of the project are to demonstrate
improvement in the image contrast and in the image quantitative accuracy that
can be obtained in monochromatic CT and to apply the system to specific
clinical research programs in neuroradiology. This paper describes the first
phantom studies carried out with a prototype system, using the dual photon
absorptiometry (DPA) method at energies of 20 and 39 keV. The results show
that improvements in image contrast and quantitative accuracy are possible
with monochromatic DPA CT. Estimates of the clinical performance of the
planned CT system are made on the basis of these initial results.

---

[1]Present address: Australian Nuclear Science and Technology Organization,

Menai, Australia.

[2]Present address: European Synchrotron Radiation Facility (ESRF), Grenoble,

France.

1

1. INTRODUCTION

We plan to use high-flux x rays from the X17 superconducting wiggler beamline at the NSLS [1] for CT imaging of the human head and neck. The project, Multiple Energy Computed Tomography (MECT) [2,3], uses a horizontal fan-shaped beam and an upright subject seated in a rotating chair. The system is expected to provide substantial improvement over conventional CT in image contrast resolution and image quantitative accuracy. The improvement comes from the lack of beam hardening [4], and the use of dual photon absorptiometry (DPA) [5], and K-edge subtraction (KES) [6] of iodine or heavier elements. Both these methods require narrow energy bands. KES of iodine with synchrotron-produced monochromatic x rays have been applied in the planar mode by Thomlinson et al. at the NSLS to transvenous coronary angiography studies in human subjects [7,8]; and in the CT mode by Thompson et al. at Stanford Synchrotron Radiation Laboratory to coronary artery imaging in an excised, inert pig heart [9].

The DPA method, in particular, is expected to provide unprecedented mapping accuracy of the concentrations of the low-Z element group and the intermediate-Z element group in the brain. The method, which involves imaging the subject at two widely separated energies, such as 40 and 100 keV, provides two separate tomographic images that reflect the concentrations of low-Z and intermediate-Z elements. Regional or global variations in the concentration of the latter group (which includes P, S, Cl, K, Ca, and Fe) are expected to be indicative of various neurological abnormalities.

A prototype system utilizing a two-crystal Si<220> monochromator and a 120-element linear array Si(Li) detector with 0.25 mm-wide elements has been developed. We present here our first images of phantoms obtained with this system.

DISCLAIMER

2. EXPERIMENTAL METHOD

We used a two crystal (Bragg-Bragg) monochromator with Si<220> crystals [10]. The right-angle monochromator design incorporates a coupled rotation and translation of the second crystal to maintain both parallelism with the first crystal and fixed exit beam height [11]. The first crystal was mounted on a water cooled copper block with In-Ga liquid metal as a thermal interface, to handle the high heat load from the X17 wiggler. The second crystal could be detuned using a piezoelectric transducer to reject higher order harmonics [10].

The DPA phantom was a 27-mm diameter Plexiglas cylinder with 5-mm diameter axial holes filled with 0-200 mmolar KOH solutions. The phantom was mounted on a precision rotation stage with an axis perpendicular to the plane of the fan beam.

Transmission of the x-ray fan beam through the phantom was measured with a cooled (-20°C) linear-array Si(Li) detector having 120 elements of 0.25 mm width and 3 mm depth each [12]. The detector currents were digitized by a multi-channel data acquisition system (DAS) utilizing voltage-to-frequency convertors [13]. The digitizer, which is currently used in the Coronary Angiography Project at the NSLS [7,8], has a dynamic range of 40,000:1 and a non-linearity of 0.02%.

3. IMAGE ACQUISITION

The data were collected for a 24-second full rotation in continuous mode. The slice thickness was 1.4 mm. The view rate was 60 s^{-1} (view stepping angle: 0.25°) which yielded 1440 views in 24 seconds.

The monochromator energy scale was determined using precise (±0.01°) crystal Bragg angle measurements and a single energy calibration at the K-edge

of iodine, 33.169 keV. The accuracy in the monochromator energy calibration is expected to be ±1%. The superconducting wiggler's magnetic field was 4.4 tesla, and the beam current during the measurements was 130-160 mA. A 3-mm thick aluminum filter was placed in front of the monochromator. The electron beam source spot dimensions were 0.90 mm FWHM horizontal width and about 0.05 mm FWHM vertical width. The source-to-subject and the subject-to-detector distances were 29 m and 1.5 m, respectively. The monochromator was detuned to provide a yield of 50%-80% of the peak yield.

To evaluate the system's in-plane spatial resolution, another 27-mm diameter cylindrical Plexiglas phantom with axial holes ranging from 0.2 mm to 0.9 mm in diameter was used. The phantom was imaged at a single energy of 20 keV with the holes empty.

4. IMAGE PROCESSING

4.1. Preliminary data processing and image corrections

Initially, the transmission values in each of the 120 pixels inside each of the 1440 views (i.e. inside each projection) were converted to attenuation values (i.e. $\mu \cdot x$ values) by dividing each transmission pixel datum by the corresponding no-subject datum (i.e. air datum) and then computing the negative logarithm of the ratio. This resulted in a sinogram of 120 x 1440 pixels. However, because of the pre-set values of the parameters in the reconstruction code, only 180° data (i.e. 720 views) were used. Next, a series of corrections was applied to the data to remove image artifacts. The artifacts were probably introduced by the following experimental imperfections:

1.   The rotation axis was not at the center of the viewing field.

2.   Several individual detector channels picked up radiofrequency

noise when the beam shutter was open.

3. Several individual detector channels exhibited a drifting pattern of their gain or pedestal between calibration and measurement.

4. The cables connecting the detector to the DAS amplifiers were 40 feet long and picked up noise.

5. The oscillations in the feedback system for the piezoelectric transducer produced a periodic fluctuation in the sinogram.

The image corrections were carried out in two steps. The corrections applied to the sinogram were the following:

a. We computed the center of gravity of each view, $CG_{j,object}$, and then fit these to a sinusoidal:

$$CG_{j,predicted} = a + b \cdot \sin(c + d \cdot j \cdot CG_{j,object})$$

Since the data were measured over 180^0 for $j=1-720$, we know $d=\pi/720$; "b" is the amplitude, and "a" is the offset of the sinusoidal, which is the position of the rotation axis. The reconstruction algorithm demands that "a" will be equal the central pixel number of each view (i.e. pixel 59). The entire sinogram was then shifted left or right by (a - 59.0) pixels to put the rotation axis on this pixel.

b. The periodic fluctuations from the feedback system were corrected by normalizing the data in each view to the air values on the two sides of each view (about 6 pixels on each side). For this purpose, an averaging and linear interpolation of the air values from both sides were applied.

c. Counts from imperfect detector channels were corrected in the sinogram by a projection smoothing method. The method is described as follows. Let the value of pixel i in view j be

5

$V(i,j)$. First calculate the pixel values for an "average" view, $V(i)$, by averaging all the views in the sinogram:

$$V(i) = \Sigma_j \, V(i,j)/N,$$

where N is the number of views. $V(i)$ should not contain much high frequency information since all features are smeared out when averaging views. We assume that the small high frequency information in $V(i)$ is from the channel-to-channel variation caused by detector drift after calibration. Next, we smooth the view $V(i)$ using a triangular filter. The smoothed function is called $VS(i)$. The difference between $VS(i)$ and the unsmoothed averaged projection $V(i)$ includes the high frequencies. Therefore we subtract this difference from the individual views:

$$V(i,j)_{new} = V(i,j)_{old} - [V(i) - VS(i)], \quad \text{for each pixel } i$$

and for each view j.

Besides the corrections to the sinogram, image filtration was also applied to the reconstructed images. Two-dimensional triangular filters and median filters were used for this purpose. This removed some of the remaining image artifacts and image random noise.

4.2. The Reconstruction Routine

The code SNARK [14] was used for tomographic reconstruction. The reconstructions were carried out using filtered backprojection in the configuration space, using a Sinc filter. The reconstructed image size was 119 x 119 pixels.

6

4.3. Evaluation of the Air Phantom Results

The 0.2 mm holes are separable in the image (Fig. 1).

4.4. Evaluation of the DPA Phantom Results

Figure 2 shows a top view of holes in the DPA phantom. The KOH concentrations in holes 1 to 5 are 200, 39.2, 7.7, 1.5 and 0.0 mM, respectively. The reconstructed images for the 20 keV and 38 keV measurements with the DPA phantom are shown in Figs. 3 and 4. The quantitative evaluation of the images is described below. Because of the artifacts in the central part of these two images, the four central holes were not taken into account in our quantitative evaluation of the results.

4.4.1. DPA formalism

Using the measured images at 20 and 38 keV, the DPA equations were used to obtain nominal tissue concentrations of the low-Z and intermediate-Z element groups. For the holes in our phantom, filled with KOH solutions, the low-Z element group consists of H and O in water, and the intermediate-Z group consists of potassium. The concentrations X_w and X_K are given by the equations:

$$X_w = (\epsilon_1 \cdot \mu_{Kh} - \epsilon_h \cdot \mu_{Kl}) / (\mu_{wl} \cdot \mu_{Kh} - \mu_{wh} \cdot \mu_{Kl}) \qquad \text{Eq. 1}$$

$$X_K = (\epsilon_1 \cdot \mu_{wh} - \epsilon_h \cdot \mu_{wl}) / (\mu_{Kl} \cdot \mu_{wh} - \mu_{Kh} \cdot \mu_{wl}) \qquad \text{Eq. 2}$$

where μ_{wl} and μ_{Kl} are the attenuation coefficients of the lower-energy x rays in water and K, respectively, and μ_{wh} and μ_{Kh} are those of the higher-energy x rays for these two substances. The values ϵ_1 and ϵ_h are the measured attenuation factors for x rays of these two energies.

4.4.2. Measurement of the attenuation coefficients

The energy bandwidth for the fundamental passed by the monochromator was less than 0.1% $\Delta E/E$. However, harmonics were allowed, and at the crystal detuning levels used in the experiment they contributed to the transmitted x-ray signals measured in the detector [15]. The harmonic contribution made the effective beam energy higher than the fundamental energy. Therefore, in the first step of our data analysis we used Figs. 3 and 4 to calculate the attenuation coefficients of the lower- and the higher-energy beams in water and potassium. For this purpose, the known values the KOH concentrations in the different holes of the phantom were used in the following way. The pixel values for each hole were averaged, and were weighted by the standard deviation of the pixel values in that particular channel to emphasis the data from "better" channels. The measured linear attenuation coefficients (in units of 1/cm) for the 20- and the 38-keV images were then plotted as functions of the KOH concentration (Figs. 5 and 6). The slopes of the linear fits in these two figures provide the potassium mass attenuation coefficients, while their value at zero KOH concentration provides the water linear attenuation coefficients. The results are summarized in Table 1.

Because of the harmonic contribution, we could not find effective beam energy values for the low- and high-energy measurements to match closely the measured attenuation coefficients for water and potassium listed in Table 1. The closer energies found, however, were 22 keV and 39 keV, for which the calculated attenuation coefficients also appear in Table 1. Deviation of the derived effective energy values (22 keV and 39 keV) from the monochromator energies is 10% for the lower energy but only 2.6% for the higher energy. This difference supports the assumption that the high harmonic contamination in the beam is the source of the deviation of the effective beam energy from the nominal value.

8

4.4.3. Derivation of the low-Z and the intermediate-Z images

The measured attenuation coefficients μ_{wl}, μ_{Kl}, μ_{wh}, and μ_{Kh} listed in Table 1, and the measured attenuation values ϵ_l and ϵ_h read from the reconstructed images in Figs. 3 and 4 were used in the DPA Equations 1 and 2 to calculate the concentrations X_w and X_K for the low-Z and the intermediate-Z element groups for each pixel. The images so derived appear in Figs. 7 and 8. Figures 9 and 10 show the averaged concentrations of these two element groups in different phantom channels as a function of the potassium concentration in the channel. As expected, the image contrast in the intermediate-Z image is proportional to the solution concentration of KOH, while the contrast in the low-Z image does not depend on the KOH concentration.

5. SUMMARY AND CONCLUSIONS

Despite several imperfections in the performance of the system components and in the data acquisition process, the two goals of monochromatic DPA technique, i.e. providing high image contrast resolution and providing fine image quantitative precision, have been achieved in the present study. From Figs. 8 and 10, one may conclude that the smallest KOH concentration detectable in this study is that of channel 3, 7.7 rM "OH. This means that 0.3 mg potassium/cc is spatially resolved in the 5-mm holes. Noting that the normal average potassium concentration in the brain is 3 mg/g, the limit of K detection in the present study is 10% of the K concentration of the normal brain.

The quantitative performance of the system is seen from the low-Z and the intermediate-Z images (Figs. 7 and 8), and from the accompanying plots (Figs. 9 and 10). In particular, the lack of correlation between the low-Z gray scale and the K concentration of the solutions (Figs. 7 and 9) emphasize

9

the quantitative capability of the method.

The design of the final MECT system for human studies includes provisions that should remove or reduce most of the experimental imperfections of the present study. These problems include harmonic contamination of the beam, fluctuations in the monochromator output, and noise and gain instability in the detector channels.

REFERENCES

[1]   W. Thomlinson, D. Chapman, N. Gmür, and N. Lazarz, "The superconducting wiggler beamport at the National Synchrotron Light Source", *Nucl. Instr. and Meth.* A266, 226-233, 1988.

[2]   F.A. Dilmanian, R.F. Garrett, W.C. Thomlinson, L.E. Berman, L.D. Chapman, N.F. Gmür, N.M. Lazarz, P.N. Luke, H.R. Moulin, T. Oversluizen, D.N. Slatkin, V. Stojanoff, A.C. Thompson, N.D. Volkow, and H.D. Zeman. *Physica Medica* VI, 301-307, 1990.

[3]   F.A. Dilmanian, R.F. Garrett, W.C. Thomlinson, L.E. Berman, L.D. Chapman, J.B. Hastings, P.N. Luke, T. Oversluizen, D.P. Siddons, D.N. Slatkin, V. Stojanoff, A.C. Thompson, N.D. Volkow, and H.D. Zeman, "Computed tomography with monochromatic x rays from the National Synchrotron Light Source", *Nucl. Instr. and Meth. in Phys. Res.* B56/57, 1208-1213, 1991.

[4]   J.P. Stonestrom, R.E. Alvarez, and A. Macovski, "A framework for spectral artifact corrections in x-ray CT", IEEE Trans. Biom. Eng. BME-28, 128-141, 1981.

[5]   C.E. Cann and H.K. Genant, "Precise measurement of vertebral mineral content using computed tomography", *J. Comp. Assisted Tom.* 4, 493-500, 1980.

[6]   W.R. Brody, A. Macovski, N.J. Pelc, L. Lehmann, R.A. Joseph, and L.S. Edelbeit, "Intravenous arteriography using scanned projection radiography", *Radiol.* 141, 509-514, 1981.

[7]   W. Thomlinson, N. Gmur, D. Chapman, R. Garrett, N. Lazarz, J. Morrison, P. Reiser, V. Padmanabhan, L. Ong, S. Green, A. Thompson, H. Zeman, R. Hofstadter, G. Brown, J. Giacomini, H. Gordon, and E. Rubenstein, "Venous Synchrotron Coronary Angiography", *LANCET* 337, 36, 1991.

11

[8] W. Thomlinson, N. Gmur, D. Chapman, R. Garrett, N. Lazarz, H. Moulin, A.C. Thompson, H.D. Zeman, G.S. Brown, J. Morrison, P. Reiser, V. Padmanabhan, L. Ong, S. Green, J. Giacomini, H. Gordon, and E. Rubenstein, "First operation of the Medical Research Facility at the NSLS for Coronary Angiography", *Rev. Sci. Instr.* 63(1), Jan. 1992 (in press).

[9] A.C. Thompson, J. Llacer, L. Campbell Finman, E.B. Hughes, J.N. Otis, S. Wilson, and H.D. Zeman, "Computed tomography using synchrotron radiation", *Nucl. Instr. and Meth. in Phys. Res.* 222, 319-323, 1984.

[10] R.F. Garrett, F.A. Dilmanian, T. Oversluizen, A. Lenhard, L.E. Berman, D. Chapman, and W. Stoeber, "A high-energy double-crystal monochromator for the X17 superconducting wiggler beam line at the NSLS", *Rev. Sci. Instr.* 63(1), Jan. 1992 (in press).

[11] J.A. Golovchenko, R.A. Levesque, and P.L. Cowan, "X-ray monochromator system for use with synchrotron radiation sources", *Rev. Sci. Instr.*, 52, 509-516, 1981.

[12] J.T. Walton, H.A. Sommer, A.C. Thompson, E.B. Hughes, and H.D. Zeman, "300-element silicon-lithium position sensitive imaging defector for angiography" *IEEE Trans. Nucl. Sci.* NS-33, 537-541, 1986.

[13] N. Nakamura, J.E. Katz, and A.C. Thompson, "A multichannel high linearity current digitizer for digital subtraction angiography", *IEEE Trans. Nucl. Sci.* NS-35, 205-208, 1988.

[14] G.T. Herman, "Image Reconstruction from Projections. The Fundamentals of Computerized Tomography", Academic Press, New York, 1980.

[15] L.D. Chapman, H. Moulin, and R.F. Garrett, "Monochromator harmonic content measurements and calculations at energies above 20 keV", *Rev. Sci. Instr.* 63(1), Jan. 1992 (in press).

Table 1

Measured and Calculated Attenuation Coefficients

Beam Energy (keV)	Linear Attenuation Coefficients for Water (1/cm)	Mass Attenuation Coefficient for K (cm^2/g)
20 (nominal)	0.744 (measured)	8.54 (measured)
38 (nominal)	0.300 (measured)	1.58 (measured)
22 (derived)	0.694 (calculated)	9.30 (calculated)
39 (derived)	0.280 (calculated)	1.54 (calculated)

FIGURE CAPTIONS

Figure 1. Reconstructed image of the high-resolution phantom. The diameter of the holes in different rows are 0.9, 0.8, 0.7, 0.6, 0.5, 0.4, 0.3 and 0.2 mm. The center-to-center distance between the holes in each row was twice the diameter of the holes in the row.

Figure 2. Pattern of the holes in the DPA phantom. The concentration of the KOH solutions in the holes are 200 mM for hole 1, 37.7 mM for hole 2, 7.7 mM for hole 3, and 1.5 mM for hole 4. Hole 5 contained distilled water.

Figure 3. Reconstructed image of the DPA phantom at 20 keV beam energy.

Figure 4. Reconstructed image of the DPA phantom at 38 keV beam energy.

Figure 5. Least-square fit of the measured attenuation coefficients in the 20-keV DPA image (Fig. 3) as a function of the KOH concentration in the holes. Results were average i c er holes with the same KOH concentrations. Dispersion of the pixels in each hole was used for weighted averaging among holes.

Figure 6. Least-square fit for the 38-keV DPA image, otherwise as in Fig. 5.

Figure 7. Image of the low-Z element group, obtained by applying the DPA equations 1 and 2 to the 20-keV and the 38-keV images shown in Figs. 3 and 4.

14

Figure 8.   Image of the intermediate-Z element group, otherwise as in Fig. 7.

Figure 9.   Least-square fit of the measured low-Z element group concentration
            in Fig. 7 as a function of KOH concentrations in the phantom holes.

Figure 10. Least-square fit of the measured intermediate-Z element group
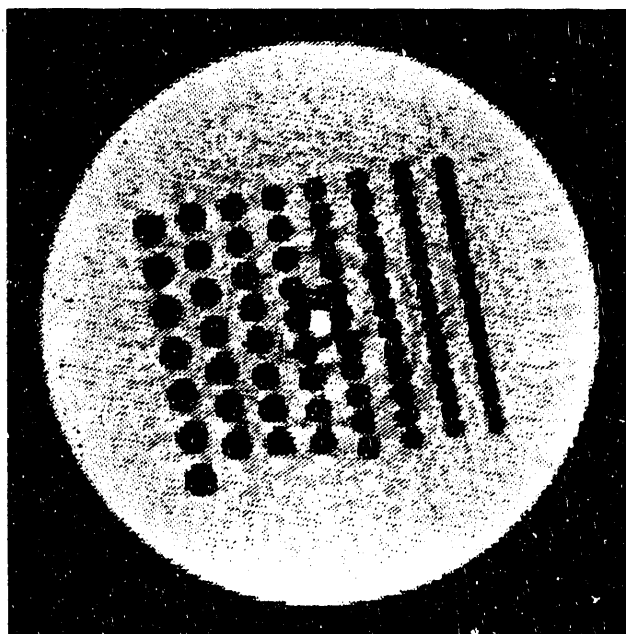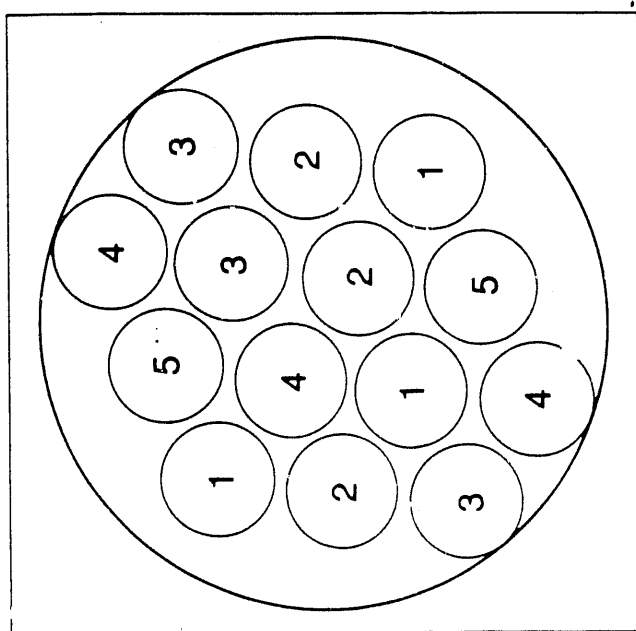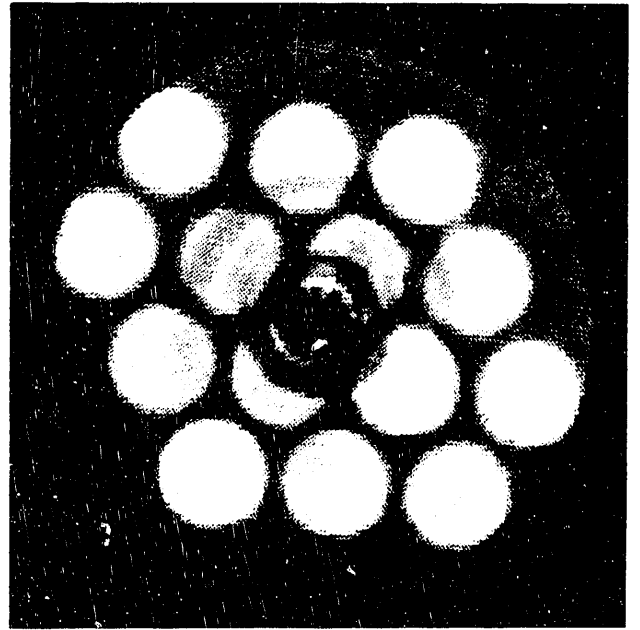   concentration, otherwise as in Fig. 9.
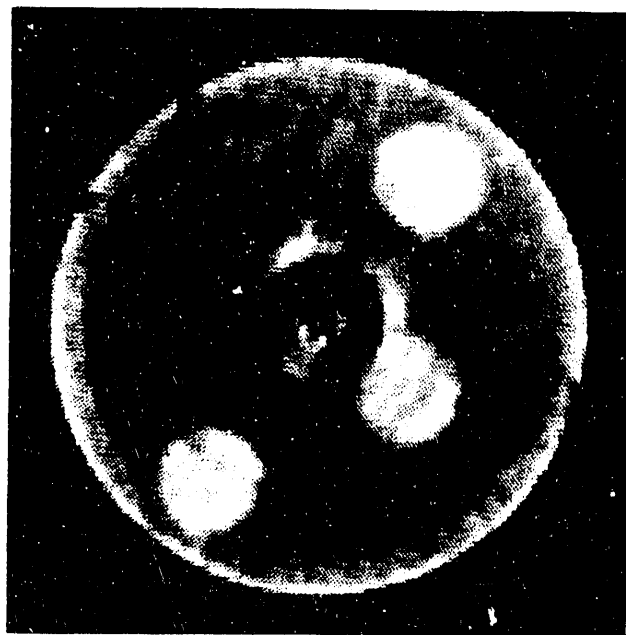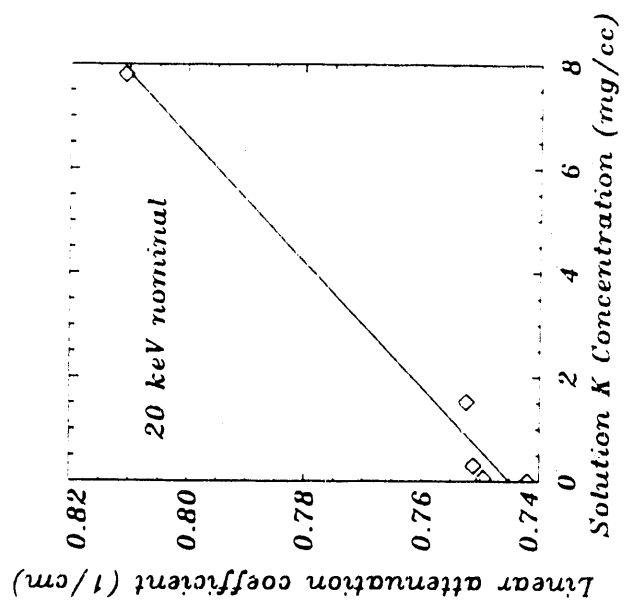
15

Fig. 1

Fig. 2

Fig. 3

Fig. 4

Fig. 5

20 keV nominal

Linear attenuation coefficient (1/cm)

0.82 0.80 0.78 0.76 0.74

Solution K Concentration (mg/cc)

0   2   4   6   8

Fig. 6

38 keV nominal

Linear attenuation coefficient (1/cm)

Solution K Concentration (mg/cc)

Fig. 7

Fig. 8

Fig. 9

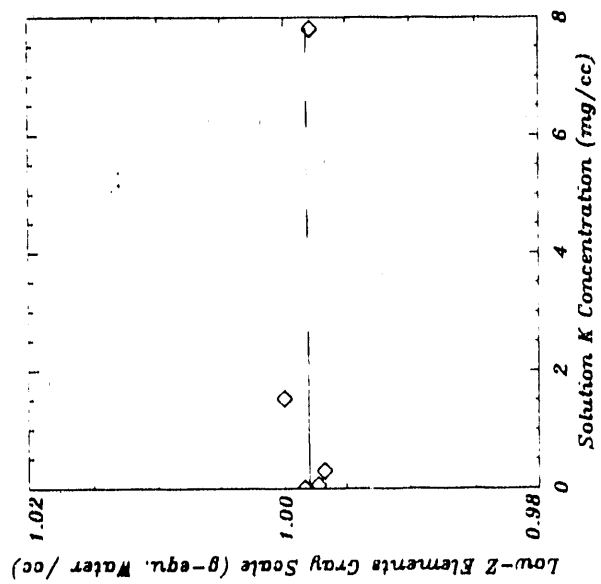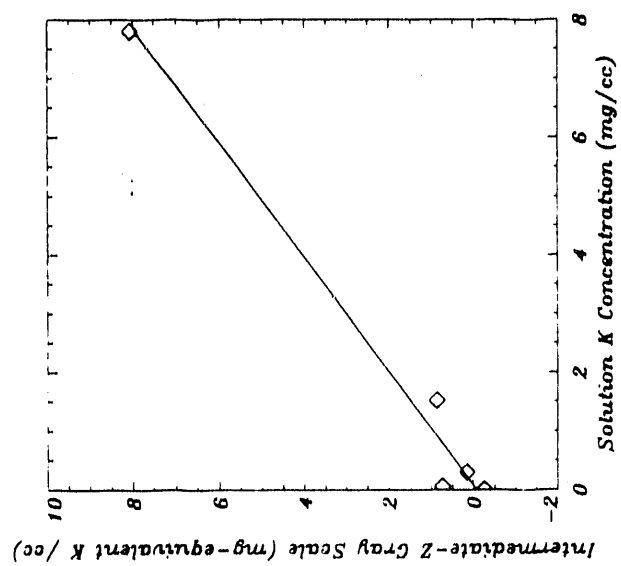Solution K Concentration (mg/cc)

Low-Z Elements Gray Scale (g-equ. Water /cc)

Fig. 10

END

DATE
FILMED
4/9/92